Article

RETRACTED: SrFe$_x$Ni$_{1-x}$O$_{3-\delta}$ Perovskites Coated on Ti Anodes and Their Electrocatalytic Properties for Cleaning Nitrogenous Wastewater

Yuqing Zhang *, Zilu Jin, Lijun Chen and Jiaqi Wang

School of Chemical Engineering and Technology, Tianjin University, Tianjin 300350, China;
a1090699180@tju.edu.cn (Z.J.); lijunchen@tju.edu.cn (L.C.); wangjiaqi1011@tju.edu.cn (J.W.)
* Correspondence: zhangyuqing@tju.edu.cn; Tel.: +86-13602077041; Fax: +86-22-27403389

check for updates

Abstract: Perovskites (ABO$_3$), regarded as the antioxidative anode materials in electrocatalysis to clean nitrogenous wastewater, show limited oxygen vacancies and conductivity due to their traditional semiconductor characteristic. To further improve the conductivity and electrocatalytic activity, the ferrum (Fe) element was first doped into the SrNiO$_3$ to fabricate the SrFe$_x$Ni$_{1-x}$O$_{3-\delta}$ perovskites, and their optimum fabrication conditions were determined. SrFe$_x$Ni$_{1-x}$O$_{3-\delta}$ perovskites were coated on a titanium (Ti) plate to prepare the SrFe$_x$Ni$_{1-x}$O$_{3-\delta}$/Ti electrodes. Afterward, one SrFe$_x$Ni$_{1-x}$O$_{3-\delta}$/Ti anode and two stainless steel cathodes were combined to assemble the electrocatalytic reactor (ECR) for cleaning simulated nitrogenous wastewater ((NH$_4$)$_2$SO$_4$ solution, initial total nitrogen (TN) concentration of 150 mg L^{-1}). Additionally, SrFe$_x$Ni$_{1-x}$O$_{3-\delta}$ materials were characterized using Fourier Transform Infrared (FT-IR), Raman spectra, X-Ray Diffraction (XRD), Energy Dispersive X-ray (EDX), Electrochemical Impedance Spectroscopy (EIS) and Tafel curves, respectively. The results indicate that SrFe$_x$Ni$_{1-x}$O$_{3-\delta}$ materials are featured with the perovskite crystal structure and Fe is appreciably doped into SrNiO$_3$. Moreover, the optimum conditions for fabricating SrFe$_x$Ni$_{1-x}$O$_{3-\delta}$ were the reaction time of 120 min for citrate sol-gel, a calcination temperature of 700 °C, and Fe doping content of $x = 0.3$. SrFe$_{0.3}$Ni$_{0.7}$O$_{2.85}$, and perovskite performs attractive electrocatalytic activity (TN removal ratio of 91.33%) and ECR conductivity of 3.62 mS cm^{-1} under an electrocatalytic time of 150 min. Therefore, SrFe$_x$Ni$_{1-x}$O$_{3-\delta}$ perovskites are desirable for cleaning nitrogenous wastewater in electrocatalysis.

Keywords: ferrum doping; SrNiO$_3$; perovskite; electrocatalysis; nitrogenous wastewater

1. Introduction

With rapid industrialization development, nitrogenous wastewater massively generated by the chemical industry, municipal engineering, and agricultural life leads to a serious threat to humankind and the ecosystem [1]. Various treatment technologies have been developed to remove the nitrogenous contaminations in wastewater, such as ion exchange [2], the biochemical method [3], breakpoint chlorination [4], and adsorption [5]. However, these treatments have some disadvantages (moderate environment, the introduction of additional chemicals in water and secondary pollution, etc.), limiting their application [6]. Electrocatalysis with the metal oxides anode has attracted widespread concerns in cleaning nitrogenous wastewater owing to its high efficiency, clean oxidation, and easy controllability [7,8]. For example, Okanishi et al. [9] used the SnO$_2$-modified Pt electrocatalyst to oxidize the ammonia and its activation energy realized 58 kJ mol^{-1}. Reyter et al. [10] removed the nitrate using the electrochemical method with the Ti/IrO$_2$ anode and NH$_3$ conversion reached 82% at a current density of 80 mA cm^{-2}. Nevertheless, the traditional coated anode relies on the noble or rare metal oxides (IrO$_2$, Ta$_2$O$_5$, RuO$_2$, et al.) [11].

Perovskites, as bimetallic oxides (ABO_3), can be used as the anodic coating in electrocatalytic processes due to their low cost, abundance, and easy modification [12,13]. In the band structure of perovskite, the conduction band is determined by the 3d orbit of the B-site element [14]. The increase of 3d electrons in the B-site element enhances the electrocatalytic activity of perovskite by virtue of more electrons remaining in an excited state (valence band). Consequently, the choice of the B-site element is extremely crucial, which destines the band structure and electrocatalytic activity of perovskite [15]. The whole system of perovskite keeps electroneutrality and satisfies the restriction of tolerance factor (*t*) shown in Equation (1).

$$t = \frac{R_A + R_O}{\sqrt{2}(R_O + R_B)} \tag{1}$$

where R_A, R_B, and R_O stand for the radiuses of A-site cation, B-site cation, and oxygen anion (O^{2-}) in the cubic perovskite structure, which can be only formed when $R_A \geq 90$ pm, $R_B \geq 51$ pm, and $0.75 \leq t \leq 1.0$ [16,17]. Meanwhile, the more closely *t* approaches 1.0, the more stable the perovskite structure is. Accordingly, the proper A-site element stabilizes the electron structure and crystal form of perovskite. Mori et al. [18] synthesized an epitaxial $La_{0.8}Sr_{0.2}CoO_3$ perovskite for the cathode, and its calculated *t* was equal to 0.8655.

Nickel (Ni) has the outermost electron configuration of $3d^8 4s^2$ with the abundant 3d electrons and empty 3d orbits among the transition metal elements (Mn: $3d^5 4s^2$, Fe: $3d^6 4s^2$, Co: $3d^7 4s^2$ and Cu: $3d^{10} 4s^1$) in the fourth period. Therefore, when Ni stands for the B-site element of ABO_3, perovskite is expected to possess excellent electrocatalytic activity and appropriate conductivity. Moreover, in nickel-based perovskite of ABO_3 (B = Ni), the strontium (Sr) element in the A-site can more strongly stabilize the cubic crystal construction of perovskite (*t* = 0.9704) compared with $LaNiO_3$ (*t* = 0.9140), $CaNiO_3$ (*t* = 0.9027) and $BaNiO_3$ (*t* = 1.034) [19]. Oxygen vacancies in perovskite can provide more active sites and hydroxyl radicals ($\cdot OH$) for electrocatalysis, significantly contributing to electron transfer during the reaction. In order to form more oxygen vacancies in $SrNiO_3$ perovskite and then enhance its electrocatalytic properties, ferrum (Fe) can be doped and partially substitute the Ni element in the B-site, because they have similar electronegativity (Fe: 1.8, Ni: 1.8) and atomic radii (Fe: 124.1 pm, Ni: 124.6 pm). Moreover, Fe (III) and Ni (IV) show different valence states in favor of delivering electrons and forming oxygen vacancies according to the electroneutrality principle [20]. Therefore, based on the above analysis, $SrFe_xNi_{1-x}O_{3-\delta}$ perovskites through doping Fe element into the $SrNiO_3$ perform the better conductivity and electrocatalytic activity.

NH_4^+ represents a common contaminant in nitrogenous wastewater and the widely accepted mechanism for removing NH_4^+ in wastewater is the electrochemical oxidation during the electrocatalysis [21]. The $\cdot OH$ can efficiently oxidize the NH_4^+ into N_2 on the anode. Zhou et al. [22] degraded the ammonia nitrogen (NH_4^+-N) in wastewater by reverse electrodialysis (RED), and NH_4^+-N removal ratio reached 25% with the initial NH_4^+-N concentration of 10 mg L^{-1}. Vlyssides et al. [23] treated the domestic wastewater (NH_4^+-N concentration of 150 mg L^{-1}, pH = 6) through electrocatalysis and NH_4^+-N was reduced by 43.3% at the residence time of 30 min. In summary, the electrocatalytic method is expected to clean the wastewater containing NH_4^+.

In this paper, to improve the conductivity and electrocatalytic activity for removing NH_4^+ during the electrocatalysis, low-cost $SrFe_xNi_{1-x}O_{3-\delta}$ perovskites were fabricated by doping Fe into $SrNiO_3$, and their optimum fabrication conditions were determined. Moreover, $SrFe_xNi_{1-x}O_{3-\delta}$ perovskites were coated on the Ti plate to prepare the $SrFe_xNi_{1-x}O_{3-\delta}$/Ti electrodes and the electrocatalytic reactor (ECR) was assembled with the $SrFe_xNi_{1-x}O_{3-\delta}$/Ti anode to clean simulated nitrogenous wastewater. Perovskite-type $SrFe_xNi_{1-x}O_{3-\delta}$ structure was testified and Fe was evidently doped into the $SrNiO_3$ matrix. Herein, $SrFe_xNi_{1-x}O_{3-\delta}$ perovskites achieve attractive total nitrogen (TN) removal ratio and conductivity, indicating that they are suitable to clean nitrogenous wastewater in electrocatalysis.

2. Experimental

2.1. Materials and Reagents

N,*N*-dimethylacetamide (DMAc, AR grade, 99.5%), acetylene black (AR grade, 99.0%) and potassium bromide (KBr, AR grade, 99.0%) were provided by Tianjin Kemiou Chemical Reagent Co., Ltd. (Tianjin, China). Polyvinylidene fluoride (PVDF, 1015) was purchased from Solvay Co., Ltd. (Shanghai, China). Ammonium sulphate ((NH_4)$_2SO_4$, AR grade, 99.0%), ferric nitrate ($Fe(NO_3)_3 \cdot 9H_2O$, AR grade, 99.5%), strontium nitrate ($Sr(NO_3)_2$, AR grade, 99.5%), nickel nitrate ($Ni(NO_3)_3 \cdot 6H_2O$, AR grade, 98.0%) and potassium persulfate ($K_2S_2O_8$, AR grade, 99.5%) were supplied by Tianjin Yuanli Chemical Engineering Co., Ltd. (Tianjin, China). Sodium hydroxide (NaOH, AR grade, 99.0%) was obtained from Tianjin Guangfu Technology Development Co., Ltd. (Tianjin, China). Citric acid ($C_6H_8O_7 \cdot H_2O$, AR grade, 99.5%) was brought from Tianjin North Tianyi Chemicals Co., Ltd. (Tianjin, China). All reagents and chemicals were used as received.

### 2.2. Fabrication of the $SrFe_xNi_{1-x}O_{3-\delta}$ Perovskites

$SrFe_xNi_{1-x}O_{3-\delta}$ perovskites are fabricated using the citrate sol-gel method, which could be clearly observed from Figure 1 [24,25]. Firstly, stoichiometric amount of corresponding metal raw materials was determined, and the molar ratio of Sr: Ni: Fe: citric acid = 1: 1−*x*: *x*: 2.5, where *x* represented the doping content of Fe (*x* = 0, 0.1, 0.2, 0.3, 0.4 and 0.5). Then metal nitrates were fully dissolved in moderate deionized water to derive metallic ions aqueous solution. The mixture of both metallic ions, aqueous solution, and citric acid gently reacted at 80 °C for an appropriate time to form citrate complexation under magnetic stirring (rotational speed of 120 rpm), then dried (120 °C, 12 h) to evaporate the excess water in citrate sol-gel. Finally, precursors of $SrFe_xNi_{1-x}O_{3-\delta}$ were calcined in a muffle furnace through a temperature-programmed route, which was linearly heated to 300 °C and maintained for 1 h, then kept at high temperature (600–750 °C) for 2 h under an air atmosphere (heating rate of 5 °C min^{-1}). The desired $SrFe_xNi_{1-x}O_{3-\delta}$ (*x* = 0, 0.1, 0.2, 0.3, 0.4 and 0.5) perovskites were obtained. In this work, the effect of reaction time for citrate sol-gel, calcination temperature, and doping content of Fe were discussed for fabricating $SrFe_xNi_{1-x}O_{3-\delta}$ perovskites.
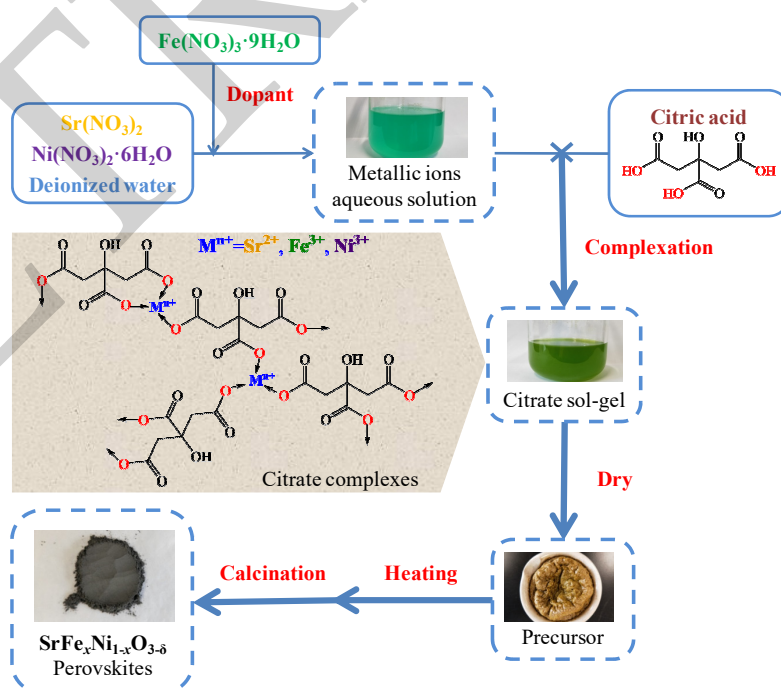
Figure 1. Schematic diagram of the fabrication process of the $SrFe_xNi_{1-x}O_{3-\delta}$ perovskites.

2.3. Preparation of the SrFe$_x$Ni$_{1-x}$O$_{3-\delta}$/Ti Anode

Preparation of the SrFe$_x$Ni$_{1-x}$O$_{3-\delta}$/Ti anode is schematically displayed in Figure 2. Firstly, a titanium (Ti) plate (Grade TA2, 80.0 mm × 17.0 mm × 1.8 mm) was polished to remove the superficial oxide layer, degreased in hot detergent, and then etched by sharp blades to produce a rough grid surface, which served as the Ti substrate [26]. Afterward, anodic materials mentioned in Table 1 (SrFe$_x$Ni$_{1-x}$O$_{3-\delta}$ perovskites, acetylene black, PVDF and DMAc in a mass ratio of 56:7:7:30) [27] were fully mixed into a viscous paste and uniformly coated on the Ti substrate with a spatula. Finally, the SrFe$_x$Ni$_{1-x}$O$_{3-\delta}$/Ti anode was prepared after being dried at 80 °C for 2 h.
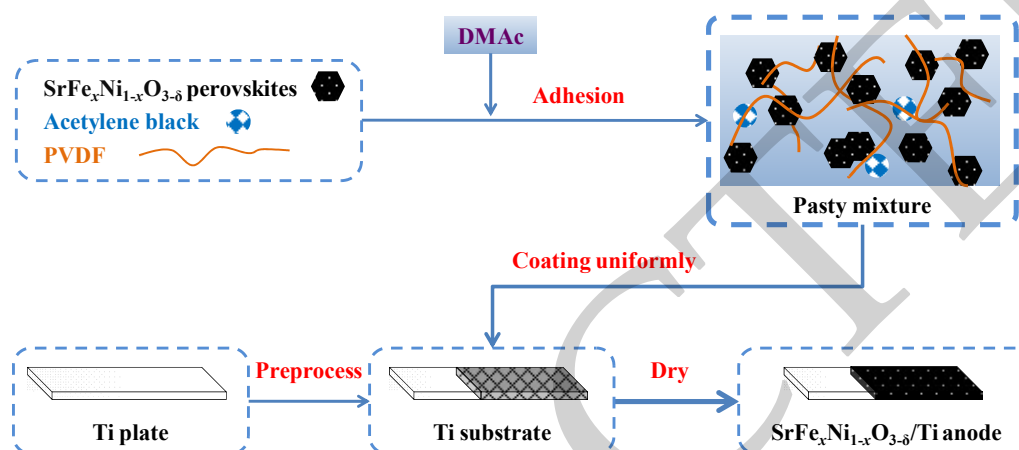
Figure 2. Schematic diagram of the preparation of the SrFe$_x$Ni$_{1-x}$O$_{3-\delta}$/Ti anode. (*N*,*N*-dimethylacetamide, DMAc; Polyvinylidene fluoride, PVDF)

Table 1. Components of materials for preparing the SrFe$_x$Ni$_{1-x}$O$_{3-\delta}$/Ti anode.

Anodic Materials	Mass Ratio (wt.%)	Function and Characteristic
SrFe$_x$Ni$_{1-x}$O$_{3-\delta}$ perovskites	56	Active material: stability, attractive electrochemical activity
Acetylene black	7	Conductor: huge specific surface area
Polyvinylidene fluoride (PVDF)	7	Binder: antioxidation, hydrophobicity
N,*N*-dimethylacetamide (DMAc)	30	Solvent: volatility, low toxicity

2.4. Assembly of Electrocatalytic Reactor (ECR)

As shown in Figure 3, the ECR was a single compartment reactor (height of 120.0 mm, bottom diameter of 93.0 mm) and constructed with one anode and two cathodes: SrFe$_x$Ni$_{1-x}$O$_{3-\delta}$/Ti as the anode and stainless steels as the cathodes. All the electrodes were vertically fixed with a constant gap (20.0 mm) and both sides of Ti substrate (effective area of 5.10 cm^2) were coated with the electrode materials. Simulated nitrogenous wastewater ((NH$_4$)$_2$SO$_4$ solution, volume of 300 mL, initial TN concentration of 150 mg L^{-1}) was intermittently poured into the ECR and forced to flow in turbulence by a magnetic stirrer (rotational speed of 120 rpm). ECR was powered just by a source of direct current (DC) connecting the amperemeter and slide rheostat with copper wires. Electrocatalytic current could be directly monitored from the amperemeter and the electrocatalytic current density was calculated by Equation (2). In addition, the electrocatalytic voltage was read by the digital multimeter between anode and cathode. The resistance, conductivity, and power density of ECR could be derived from Equations (3)–(5), respectively.

$$i = \frac{I}{S} \tag{2}$$

$$r = \frac{U}{I} \tag{3}$$

$$\kappa = \frac{L}{r \times S} \tag{4}$$

$$P = U \times i \tag{5}$$

where I is the electrocatalytic current (A), U is the electrocatalytic voltage (V), S is the effective surface area of anode (cm^2), L is the gap between anode and cathode (cm), r is the resistance of ECR (Ω), κ is the conductivity of ECR (mS cm^{-1}), P is the electrocatalytic power density of ECR (mW cm^{-2}), and i is the electrocatalytic current density of anode (mA cm^{-2}). Current density mentioned in this paper referred to the electrocatalytic current density of anode and all the experimental results were measured at 25 ± 2 °C.
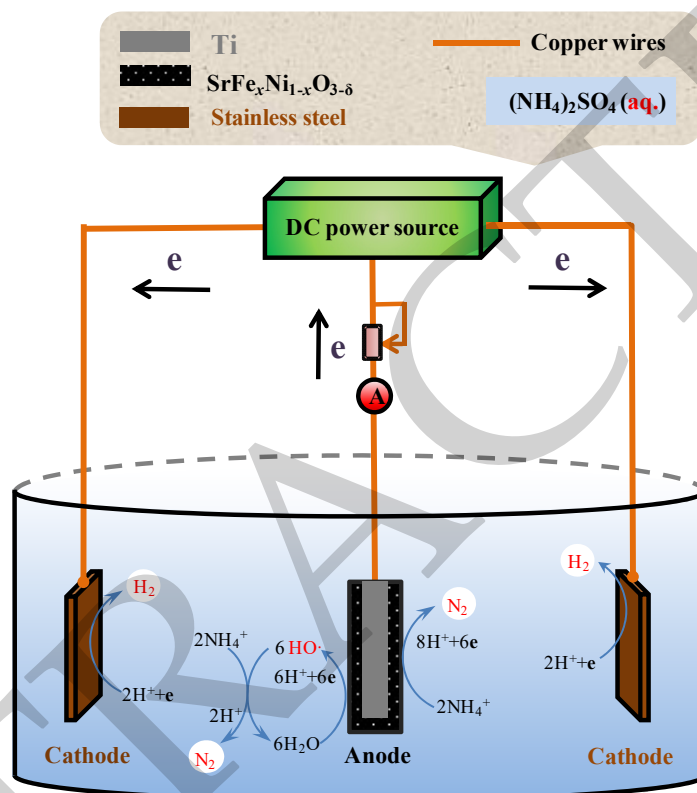
Figure 3. Schematic diagram of the electrocatalytic reactor (ECR).

2.5. Measurement of Total Nitrogen (TN) Concentration

(NH$_4$)$_2$SO$_4$ solution was selected as the simulated nitrogenous wastewater in various TN concentrations [28]. According to the discharge standard of pollutants for municipal wastewater treatment plant in China (GB 18918-2002, Class I-A Standard [29]), the TN concentrations before and after treatment by ECR were set as 150 mg/L and $\leq$ 15 mg/L, respectively. The TN concentration was determined by the alkaline potassium persulphate digestion UV spectrophotometric method (HJ 636-2012 [30]), whose details were provided in the Supplementary Information (Figure S1 and Table S1). The TN removal ratio was calculated by Equation (6):

$$R = \frac{C_0 - C}{C_0} \times 100\% \tag{6}$$

where R is the TN removal ratio (%), C_0 and C are the TN concentrations (mg L^{-1}) of the nitrogenous wastewater before and after treatment, respectively.

2.6. Characterizations and Analysis Methods

2.6.1. Scanning Electron Microscope (SEM) and Energy Dispersive X-ray (EDX) Studies

Samples were sputtered with gold and their superficial morphologies were observed under the S4800 SEM (Hitachi, Tokyo, Japan) with a resolution of 1 nm. In addition, the relative content of elements in $SrFe_xNi_{1-x}O_{3-\delta}$ was analyzed by EDX system coupled with the SEM.

2.6.2. Fourier Transform Infrared (FT-IR) Studies

$SrFe_xNi_{1-x}O_{3-\delta}$ perovskite powders of 1 mg were dried, pressed into the pellets with KBr of 100 mg, and then preserved under vacuum. The FT-IR spectra of $SrFe_xNi_{1-x}O_{3-\delta}$ perovskite pellets were collected on an Avatar 370 spectrometer (Thermo Nicolet Corp., Billerica, GA, USA) with a wavelength coverage of 400–4000 cm^{-1} and a resolution of 0.1 cm^{-1}.

2.6.3. Raman Analysis

The Raman spectra of $SrFe_xNi_{1-x}O_{3-\delta}$ materials were recorded using a high-resolution HR800 Raman spectrometer (Horiba, Montpellier, France) with a 532 nm laser beam as a light source. The laser was incident on the samples in a 2 μm diameter spot through a standard ×50 microscope objective lens and the accumulation time was 60 s for spectral measurement. The baseline of the Raman spectra was corrected with a silicon wafer.

2.6.4. X-Ray Diffraction (XRD) Studies

All the $SrFe_xNi_{1-x}O_{3-\delta}$ samples were tested on a Bruker D8 Advance diffractometer (Bruker, Karlsruhe, Germany) using Cu Kα (λ = 0.154184 nm) radiation source filtered by a Ni thin plate. The XRD data were collected over the range of 2θ = 10–80°.

2.6.5. Electrochemical Studies

Electrochemical studies were carried out in the Reference 3000 electrochemical workstation (Gamry, Warminster, America) equipped with a three-electrode system. $SrFe_xNi_{1-x}O_{3-\delta}$ materials of 1.8 mg were dispersed with ethanol of 2 mL and 0.5% Nafion of 0.05 mL under ultrasound, then the mixtures were dropped on the rotating disk electrode (RDE710, electrode area of 0.19625 cm^2, rotating speed of 1000 rpm), which were dried and served as the working electrodes. The reference electrode and counter electrode were the saturated calomel electrode (SCE) and platinum wire, respectively. Electrochemical tests, including Electrochemical Impedance Spectroscopy (EIS) and Tafel curve, were studied in Na_2SO_4 (0.5 mol L^{-1}) electrolyte solution under air atmosphere. The Tafel curve was performed with the sweep rate of 10 mV s^{-1} in a potential range from open potential to 0.6 V. EIS was performed with an amplitude of 5 mV from 100 kHz to 0.01 Hz. The relationship between current density and overpotential satisfies Equation (7), which can be applied and deduced into the low range of overpotential to calculate the value of exchange current density.

$$\eta = a + b \times \log i \tag{7}$$

where η was the overpotential (mV) and i was the current density. When η = 0, the exchange current density (i_0) could be deduced.

3. Results and Discussion

3.1. Optimum Fabrication Conditions of SrFe$_x$Ni$_{1-x}$O$_{3-\delta}$ Materials

The appropriate conditions of ECR, namely the $SrFe_xNi_{1-x}O_{3-\delta}$ perovskites amount of 0.09804 g cm^{-2} coated on the anode, current density of 11.76 mA cm^{-2} and electrocatalytic time of 30 min, are determined in the Supplementary Information (Figures S2 and S3). Based on the above

conditions of ECR, optimum fabrication conditions of $SrFe_xNi_{1-x}O_{3-\delta}$ perovskites (reaction time for citrate sol-gel, calcination temperature and doping content of Fe in $SrFe_xNi_{1-x}O_{3-\delta}$) need to be further confirmed and their electrocatalytic properties are studied in cleaning the nitrogenous wastewater. Moreover, the chemical formulas and oxygen vacancy values (δ) of $SrFe_xNi_{1-x}O_{3-\delta}$ perovskites with different doping content values (x) can be determined by the electroneutrality.

3.1.1. Effect of Reaction Time for Citrate Sol-Gel on Electrocatalytic Properties of $SrFe_xNi_{1-x}O_{3-\delta}$

During the fabrication of $SrFe_xNi_{1-x}O_{3-\delta}$ perovskites (calcination temperature of 700 °C), the effect of reaction time for citrate sol-gel on the electrocatalytic properties (TN removal ratio and conductivity of ECR) is illustrated in Figure 4. Obviously, TN removal ratio and the conductivity of ECR improve along with the reaction time for citrate sol-gel from 30–120 min, and then basically remain unchanged over 120 min. The results suggest the complexation between citric acid and metallic ions (Sr^{2+}, Ni^{3+}, and Fe^{3+}) gradually increases in the citrate sol-gel, which is beneficial to fabricate the $SrFe_xNi_{1-x}O_{3-\delta}$ perovskites and promote their electrocatalytic properties within 120 min. Moreover, among the $SrFe_xNi_{1-x}O_{3-\delta}$ (x = 0, 0.1, 0.2, 0.3, 0.4 and 0.5) materials, $SrFe_{0.3}Ni_{0.7}O_{2.85}$ achieves the superior TN removal ratio (56.20%) and conductivity of ECR (3.62 mS cm^{-1}) at the reaction time of 120 min for citrate sol-gel. Thus, the optimum reaction time for citrate sol-gel is chosen as 120 min, over which the conductivity of ECR and the TN removal ratio have no obvious improvements.
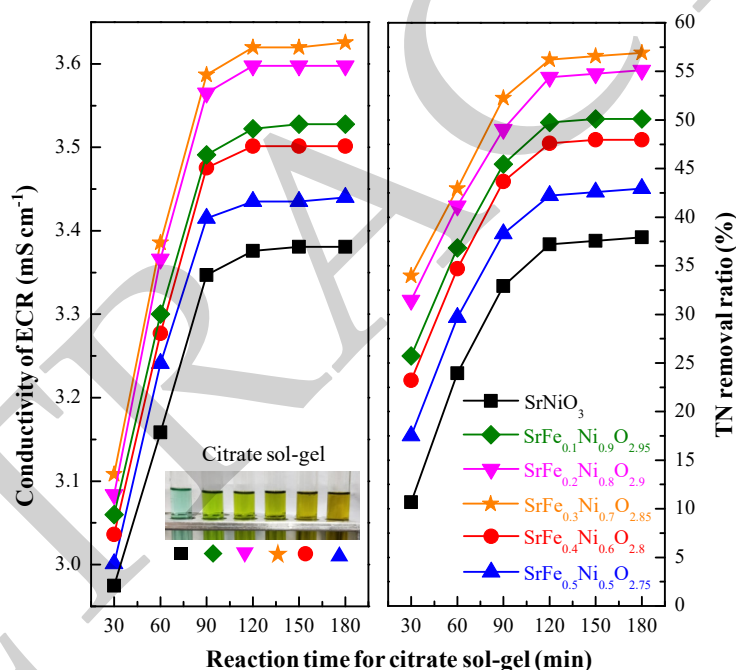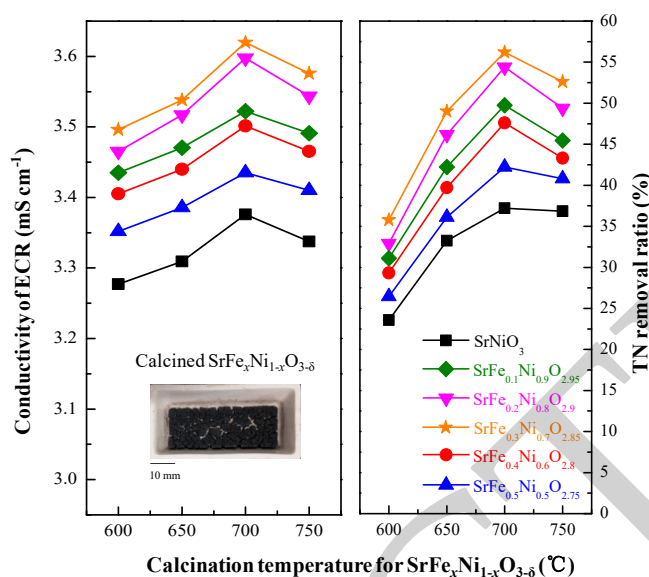

Figure 4. The effect of reaction time for citrate sol-gel on the electrocatalytic properties of $SrFe_xNi_{1-x}O_{3-\delta}$.

3.1.2. The Effect of Calcination Temperature on the Electrocatalytic Properties of $SrFe_xNi_{1-x}O_{3-\delta}$

In light of the reaction time of 120 min for the citrate sol-gel, the effect of calcination temperature on the electrocatalytic properties of $SrFe_xNi_{1-x}O_{3-\delta}$ clearly presents in Figure 5. With improving the calcination temperature for $SrFe_xNi_{1-x}O_{3-\delta}$, both the conductivity of ECR and the TN removal ratio firstly increase and then drop, of which the peak values appear at 700 °C. This is because the $SrFe_xNi_{1-x}O_{3-\delta}$ materials gradually form and stabilize the perovskite-type structure when their calcination temperatures increase from 600–700 °C. However, in terms of $SrFe_xNi_{1-x}O_{3-\delta}$ materials, higher calcination temperatures (750 °C) probably destroy their crystal structure and framework [31]. Similarly, among the $SrFe_xNi_{1-x}O_{3-\delta}$ (x = 0, 0.1, 0.2, 0.3, 0.4 and 0.5) materials, $SrFe_{0.3}Ni_{0.7}O_{2.85}$ achieves superior electrocatalytic activity (TN removal ratio of 56.20%) and ECR conductivity of

3.62 mS cm^{-1} at the calcination temperature of 700 °C. Thereby, the optimum calcination temperature for fabricating SrFe$_x$Ni$_{1-x}$O$_{3-\delta}$ materials is considered as 700 °C.

Figure 5. The effect of calcination temperature on the electrocatalytic properties of SrFe$_x$Ni$_{1-x}$O$_{3-\delta}$.

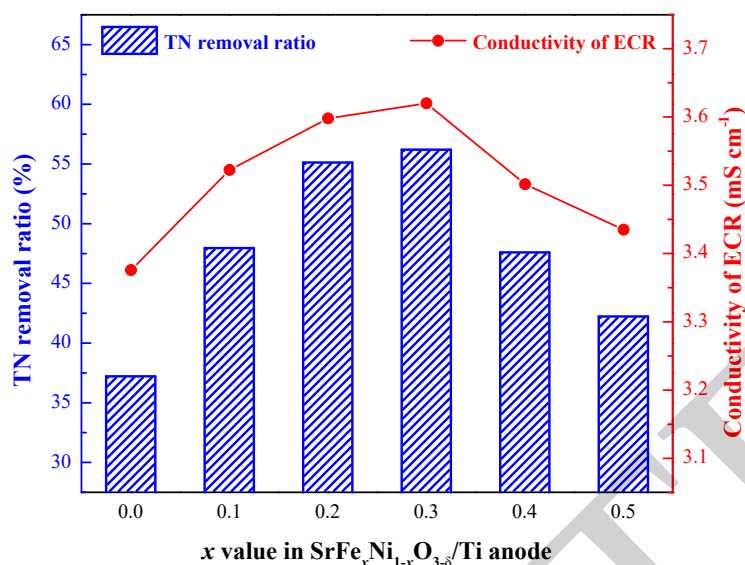### 3.1.3. The Effect of the Doping Content of Fe in SrFe$_x$Ni$_{1-x}$O$_{3-\delta}$ on Electrocatalytic Properties

With regard to the optimum fabrication conditions (reaction time of 120 min for citrate sol-gel and a calcination temperature of 700 °C), the SrFe$_x$Ni$_{1-x}$O$_{3-\delta}$ materials with different doping contents of Fe (x value) were coated on the anode in ECR, and their electrocatalytic properties were recorded in Table 2. The electrocatalytic voltage and power density of ECR with SrFe$_x$Ni$_{1-x}$O$_{3-\delta}$/Ti anode firstly drop and then ascend, raising the x. Additionally, both the TN removal ratio and conductivity of ECR give the inverse tendency plotted in Figure 6 that results from the increase of oxygen vacancies and the decline of t with the increase of x in SrFe$_x$Ni$_{1-x}$O$_{3-\delta}$ perovskites. Among the SrFe$_x$Ni$_{1-x}$O$_{3-\delta}$ ($x = 0$, 0.1, 0.2, 0.3, 0.4 and 0.5) materials, SrFe$_{0.3}$Ni$_{0.7}$O$_{2.85}$ has the highest conductivity of ECR (3.62 mS cm^{-1}) and TN removal ratio (56.20%), manifesting its superior conductivity and electrochemical activity. Therefore, the optimum doping content of Fe in SrFe$_x$Ni$_{1-x}$O$_{3-\delta}$ is $x = 0.3$.

Table 2. The effect of different anodes in ECR for cleaning nitrogenous wastewater.

SrFe$_x$Ni$_{1-x}$O$_{3-\delta}$ Coated on the Anode	Voltage (V)	Power Density (mW cm^{-2})	Conductivity of ECR (mS cm^{-1})	TN Removal Ratio (%)
SrNiO$_3$	6.97	82.0	3.38	37.21
SrFe$_{0.1}$Ni$_{0.9}$O$_{2.95}$	6.68	78.6	3.52	49.75
SrFe$_{0.2}$Ni$_{0.8}$O$_{2.9}$	6.54	76.9	3.60	54.41
SrFe$_{0.3}$Ni$_{0.7}$O$_{2.85}$	6.50	76.4	3.62	56.20
SrFe$_{0.4}$Ni$_{0.6}$O$_{2.8}$	6.72	79.1	3.50	47.60
SrFe$_{0.5}$Ni$_{0.5}$O$_{2.75}$	6.85	80.6	3.43	42.23

Total nitrogen (TN); Electrocatalytic Reactor (ECR).

Figure 6. The effect of Fe doping content (*x* value) in SrFe$_x$Ni$_{1-x}$O$_{3-\delta}$ on the electrocatalytic properties.

In the SrFe$_x$Ni$_{1-x}$O$_{3-\delta}$ perovskites, electron exchange process of B-site elements takes place due to different ionic valence states between Fe (III) and Ni (IV), promoting the electronic and conductivity and the electron transmission capacity. Meanwhile, the Fe element has more empty 3d orbits (Fe: $3d^64s^2$, four empty 3d orbits) and can be beneficial to deliver the electrons as compared with the Ni element (Ni: $3d^84s^2$, two empty 3d orbits) in the B-site. With raising the *x*, low-valent substitution in the B-site increases the oxygen vacancies according to the electroneutrality, which can also improve the ionic conductivity and electrocatalytic reactivity of SrFe$_x$Ni$_{1-x}$O$_{3-\delta}$ perovskites. However, the large *x* value relates to the low *t* value, which consequently leads to the oxygen octahedral distortion of perovskite owing to the Jahn-Teller effect, and the deviation from the standard cubic crystal structure conversely decreases the electrocatalytic reactivity and conductivity by doping [32,33].

The relationship of the *x* value in SrFe$_x$Ni$_{1-x}$O$_{3-\delta}$ perovskite materials and their characteristic parameters (oxygen vacancy value (δ), tolerance factor (*t*), and 3d electron number in the B-site) is clearly shown in Figure 7. The increasing *x* value in SrFe$_x$Ni$_{1-x}$O$_{3-\delta}$ naturally raises the oxygen vacancy value (δ) in accordance with the electroneutrality principle, which significantly avails to provide more electrocatalytic active sites and oxidative ·OH, as well as to enhance the conductivity in the perovskite. Oppositely, both the *t* value and 3d electron number in the B-site decreases with the *x* value in SrFe$_x$Ni$_{1-x}$O$_{3-\delta}$ perovskite materials, limiting their electrocatalytic activity and conductivity. The *t* values of SrFe$_x$Ni$_{1-x}$O$_{3-\delta}$ materials are totally over 0.92 (*t* = 0.9704–0.9296) and in the range of tolerance factor restriction (0.75 $\leq$ *t* $\leq$ 1.0), agreeing with the characteristic of the perovskite structure. From the results and analysis, the optimum *x* value in SrFe$_x$Ni$_{1-x}$O$_{3-\delta}$ perovskites (*x* = 0.3) reveals the balance among oxygen vacancy, 3d electron number in the B-site, and the tolerance factor of the perovskite.
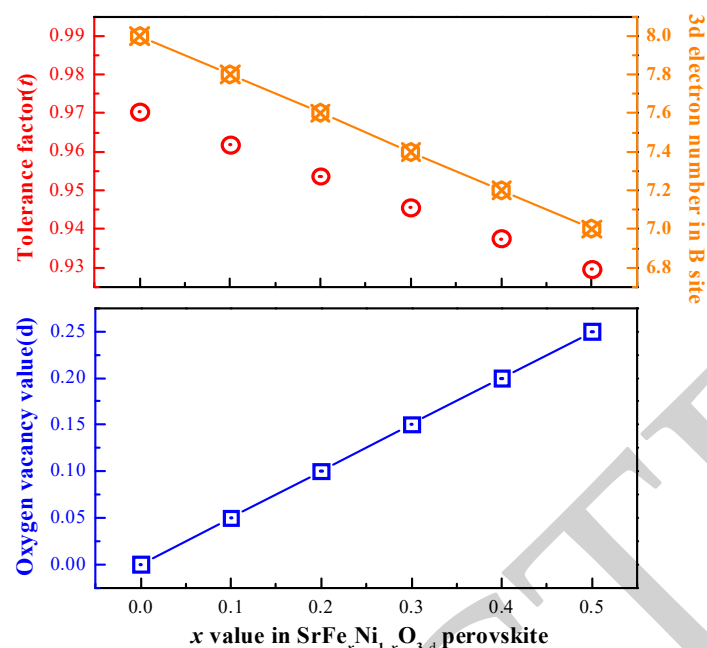
Figure 7. Characteristic parameters of $SrFe_xNi_{1-x}O_{3-\delta}$ perovskites: Oxygen vacancy value (δ), tolerance factor (t), and 3d electron number in the B-site.

3.2. The Effect of Electrocatalytic Time on TN Concentration

In order to investigate the effect of electrocatalytic time and further decrease the TN concentration of wastewater to a lower level, ECR with the $SrFe_{0.3}Ni_{0.7}O_{2.85}$/Ti anode (current density of 11.76 mA cm^{-2} and $SrFe_xNi_{1-x}O_{3-\delta}$ materials amount of 0.09804 g cm^{-2}) is applied to treat the nitrogenous wastewater under the optimum conditions for fabricating $SrFe_xNi_{1-x}O_{3-\delta}$ materials (reaction time of 120 min for citrate sol-gel and calcination temperature of 700 °C). TN concentrations are measured at the corresponding electrocatalytic time, and their variation trend is shown in Figure 8. With the increase of electrocatalytic time, TN concentration of wastewater in ECR gradually declines and reaches below 15 mg L^{-1} at an electrocatalytic time of 150 min. At the same time, wastewater treated by ECR satisfies the discharge standard of pollutants for municipal wastewater treatment plants in China (GB 18918-2002 [29], Class I-A Standard, TN $\leq$ 15 mg L^{-1}) with a TN removal ratio of 91.33% (from 150 mg L^{-1} to 14.62 mg L^{-1}). In the range of low TN concentrations (15–60 mg L^{-1}), the variation trend of the TN concentration with the electrocatalytic time is evidently slow, possibly contributing from the reduction of the concentration driving force for limiting the electrocatalytic efficiency. On the aspect of the wastewater quality standard, the appropriate electrocatalytic time can be chosen as 150 min, over which the nitrogenous wastewater treated by ECR meets the discharge standard of pollutants for municipal wastewater treatment plants in China (GB 18918-2002 [29], Class I-A Standard, TN $\leq$ 15 mg L^{-1}). In conclusion, the optimum operating conditions and performance of ECR with $SrFe_xNi_{1-x}O_{3-\delta}$/Ti anode are summarized in Table 3.
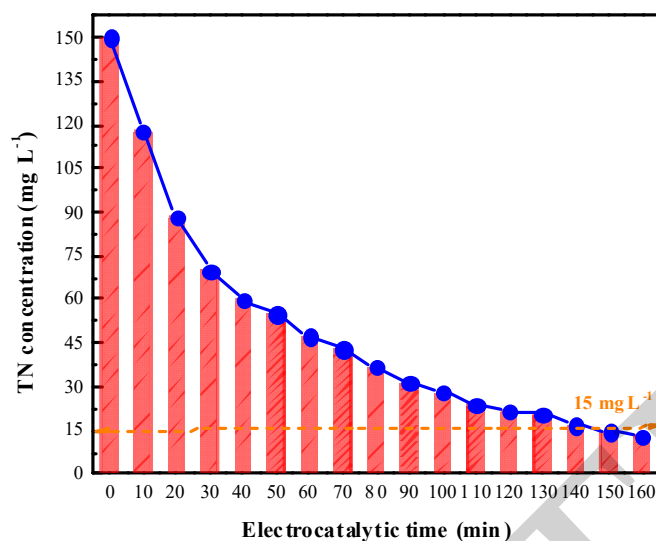
Figure 8. The effect of electrocatalytic time on TN concentration.

Table 3. The optimum operation conditions and performance of ECR with the $SrFe_xNi_{1-x}O_{3-\delta}$/Ti anode.

| Item	Value
Anode	$SrFe_xNi_{1-x}O_{3-\delta}$/Ti, 80.0 mm × 17.0 mm × 1.8 mm
Cathode	Stainless steel, 50.0 mm × 20.0 mm × 1.0 mm
Electrode gap	20.0 mm
Effective surface area of anode	5.10 cm^2
Perovskite amount coated on the anode	0.09804 g cm^{-2}
Electrocatalytic current identity	11.76 mA cm^{-2}
Perovskite material for the anode of ECR	$SrFe_{0.3}Ni_{0.7}O_{2.85}$
Reaction time for citrate sol-gel	120 min
Calcination temperature for $SrFe_xNi_{1-x}O_{3-\delta}$	700 °C
Conductivity	3.62 mS cm^{-1}
Initial TN concentration in wastewater	150 mg L^{-1}
TN removal ratio	91.33%
Treatment time	150 min
Treatment volume	300 mL

3.3. Characterization of $SrFe_xNi_{1-x}O_{3-\delta}$

$SrFe_xNi_{1-x}O_{3-\delta}$ (x = 0, 0.1, 0.2, 0.3, 0.4 and 0.5) materials were fabricated under the optimum conditions (reaction time of 120 min for citrate sol-gel and calcination temperature of 700 °C). Then the corresponding $SrFe_xNi_{1-x}O_{3-\delta}$ materials were characterized as described below.

3.3.1. SEM Studies of $SrFe_xNi_{1-x}O_{3-\delta}$ and $SrFe_xNi_{1-x}O_{3-\delta}$/Ti Anodes

According to the optimum doping content of Fe (x = 0.3) for $SrFe_xNi_{1-x}O_{3-\delta}$ materials, $SrFe_{0.3}Ni_{0.7}O_{2.85}$ has decent electrocatalytic properties. Furthermore, $SrFe_{0.3}Ni_{0.7}O_{2.85}$ material and the anodic materials of the $SrFe_{0.3}Ni_{0.7}O_{2.85}$/Ti anode are characterized through SEM and their surface morphologies are shown at different magnifications (Figure 9). $SrFe_{0.3}Ni_{0.7}O_{2.85}$ material exhibits the blocky solid-solution shape (particle size of 10–100 μm) in Figure 9a,b, triggered by high calcination temperature and lasting calcination time during the fabrication process. In addition, the clear cracks of $SrFe_{0.3}Ni_{0.7}O_{2.85}$ material can be also observed from Figure 9a. Moreover, Figure 9c,d show the adhesive phenomena and roughness on the coated surface of $SrFe_{0.3}Ni_{0.7}O_{2.85}$/Ti anode, of which the loose morphology facilitates the mass transfer and the contact between contaminants and electrode surface.
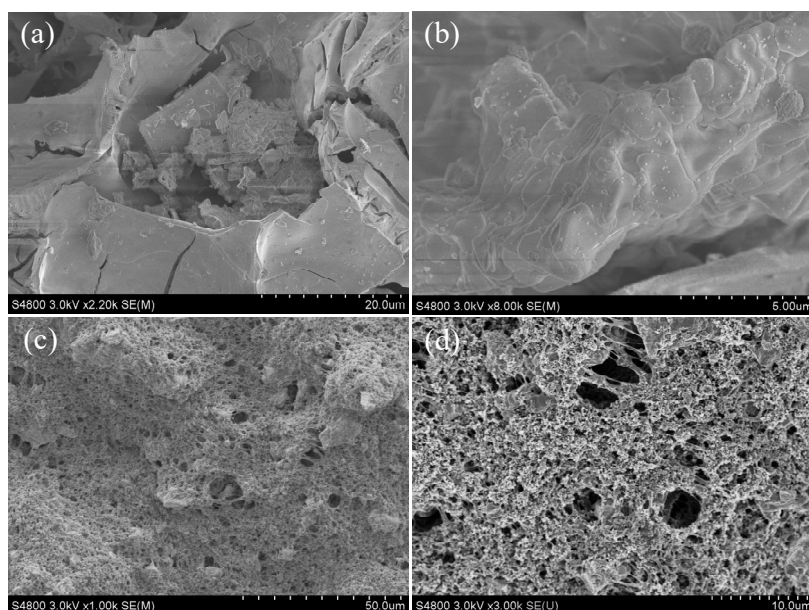
Figure 9. SEM images of (**a**,**b**) $SrFe_{0.3}Ni_{0.7}O_{2.85}$ and (**c**,**d**) the surface of $SrFe_{0.3}Ni_{0.7}O_{2.85}$/Ti anode.

3.3.2. FT-IR and Raman Analysis of $SrFe_xNi_{1-x}O_{3-\delta}$

FT-IR spectra of perovskite-type $SrNiO_3$ and $SrNiO_3$ precursor were displayed in Figure 10. The $SrNiO_3$ precursor was fabricated without the heat treatment and calcination process and the $SrNiO_3$ perovskite was subsequently fabricated after heating and calcining the $SrNiO_3$ precursor. In accordance with the literature [34,35], the wide and intensive absorption peak approximately ranging from 3000–3500 cm^{-1} can be assigned to the stretching vibration of O–H. Characteristic adsorption peaks at 640 cm^{-1}, 895 cm^{-1}, and 1074 cm^{-1} represent the C–H vibration. Meanwhile, the peaks of 1388 cm^{-1} and 1589 cm^{-1} belong to the stretching vibration of COO^-, mainly contributing from the residual citric acid in the $SrNiO_3$ precursor. Furthermore, the out-plane vibration of 812 cm^{-1} can be ascribed to nitrate radicals in the raw reagent.
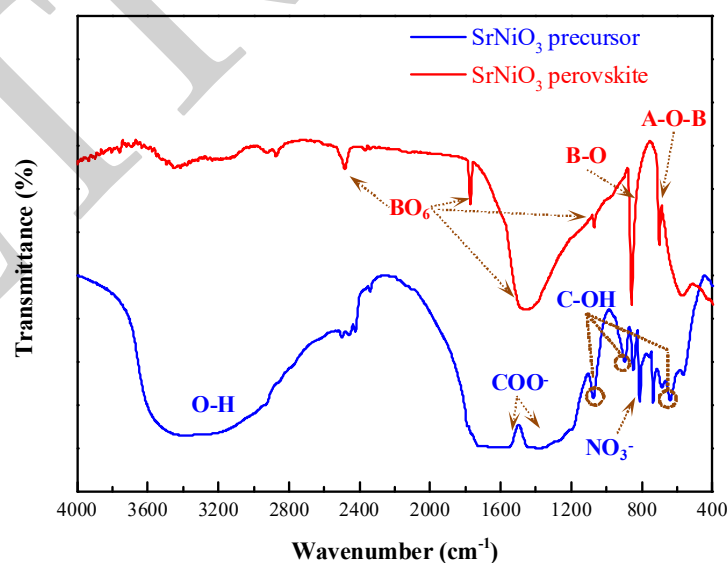
Figure 10. FT-IR spectra of $SrNiO_3$ perovskite and $SrNiO_3$ precursor.

As shown in Figure 11a, all the $SrFe_xNi_{1-x}O_{3-\delta}$ materials basically perform the same tendency in the FT-IR spectra. The low-frequency adsorption of 570 cm^{-1} possibly results from translational motion between the A-site cation and BO_6 octahedron, suggesting the ionic vibration environment

of the A-site element [36]. The intensive absorption band appearing at 735 cm^{-1} can be ascribed to the A-O-B stretching vibration and it is slightly split into two peaks in Fe-doped $SrNiO_3$ due to the B-site difference of the ionic radius and the valence state [37]. The well-resolved peak of 858 cm^{-1} is considered to belong to the B–O stretching in perovskite compounds [38]. In addition, the vibrational peaks at the high-frequency region can be assigned to the asymmetric stretch (1450 cm^{-1}, 2482 cm^{-1}) and bend (1068 cm^{-1}, 1770 cm^{-1}) of the BO_6 octahedra [39]. The absorption peak of Fe_2O_3 is not detected in the FT-IR spectroscopy, indicating that Fe element does center into the lattice of $SrNiO_3$ perovskite. Moreover, the doping of the Fe element has not changed the perovskite framework structure, and its doping content (x) in $SrFe_xNi_{1-x}O_{3-\delta}$ can reach $x = 0.5$.

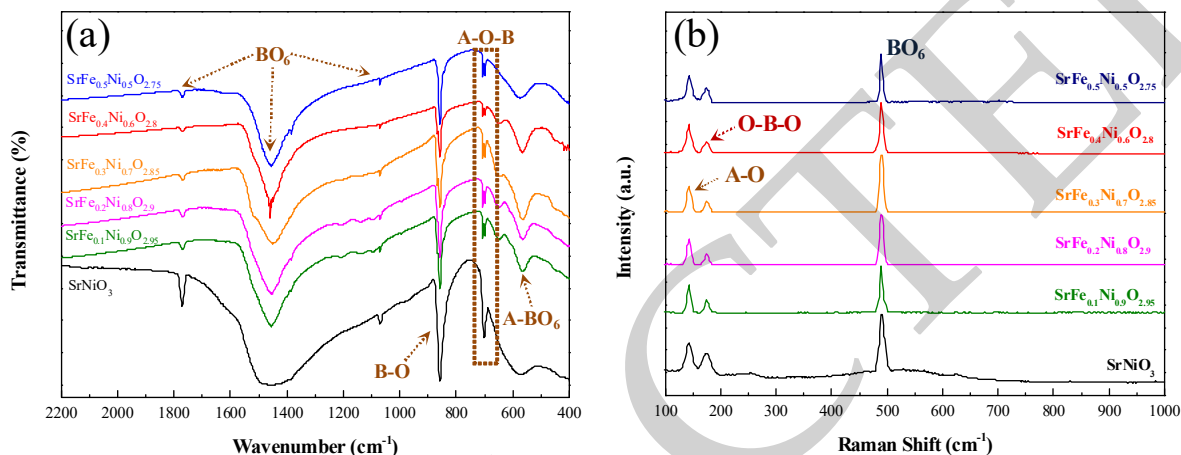**Figure 11.** FT-IR (**a**) and Raman (**b**) spectra of $SrFe_xNi_{1-x}O_{3-\delta}$.

The Raman spectra of $SrFe_xNi_{1-x}O_{3-\delta}$ are exhibited in Figure 11b. The Raman active mode located around 143 cm^{-1} is associated with the vibration of the oxygen ion and A-site cation, reflecting the Raman information of Sr–O [40]. The mode appearing at 174 cm^{-1} is related to the bending vibration of oxygen and B-site cation, proving the occurrence of O–Ni–O and O–Fe–O in perovskite [41]. The Raman peak at 489 cm^{-1} is assigned to the breathing vibration of oxygen in (Ni/Fe)O_6 octahedra, which is sensitive to the B-site substitution [42]. The Raman spectra can clearly identify the effect of B- and the A-site cations, which contributes to the perovskite structure of ABO_3.

3.3.3. XRD Analysis of $SrFe_xNi_{1-x}O_{3-\delta}$

Further refined characterization of $SrFe_xNi_{1-x}O_{3-\delta}$ materials is conducted by XRD analysis in Figure 12. All the XRD diffraction peaks emerging at 29.6°, 32.8°, 37.3°, 44.1°, 43.4°, and 62.9° are sharp and intensive, certifying the brilliant crystallinity of $SrFe_xNi_{1-x}O_{3-\delta}$ materials. Above all, XRD patterns are featured with pure perovskite-type $SrNiO_3$ (PDF#28-1242) and the doping of Fe element does not change the single perovskite phase [43,44], which agrees with the FT-IR and Raman analysis. No diffraction peaks of Fe_2O_3, Fe_3O_4, NiO, SrO or other impurities can be observed in the XRD patterns, demonstrating that Fe element is successfully doped into the crystal lattice of perovskite-type structure [45]. According to the results of analysis software (Jade 6.5), the average crystallite sizes are in the range of 432–485 nm for the $SrFe_xNi_{1-x}O_{3-\delta}$ materials. Moreover, the FWHM (full width at half maximum) value for the XRD patterns of $SrFe_xNi_{1-x}O_{3-\delta}$ materials is calculated as 0.332 at the sharpest XRD peak (2θ = 32.8°), which is located in the range (0.1–0.5) of the common crystal material (α-quartz, mica, corundum, diamond, et al.).

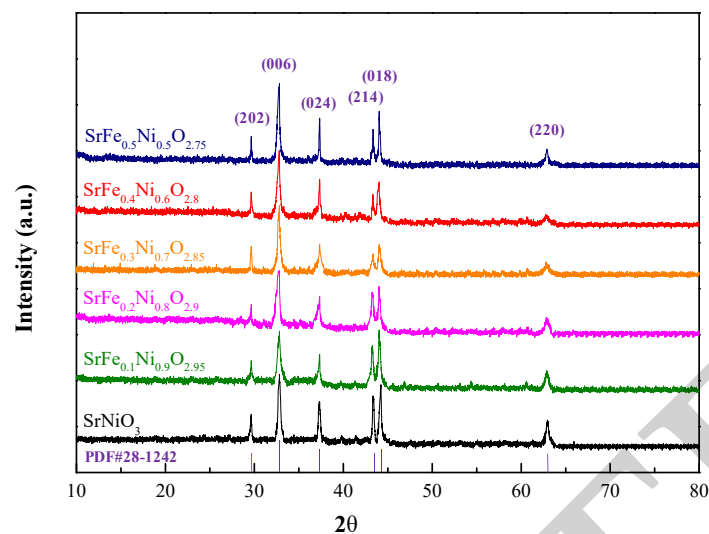**Figure 12.** XRD patterns of $SrFe_xNi_{1-x}O_{3-\delta}$.

3.3.4. EDX Analysis of $SrFe_xNi_{1-x}O_{3-\delta}$

Figure 13 shows the EDX spectrum of $SrFe_{0.3}Ni_{0.7}O_{2.85}$ perovskite, in which the Sr, Ni, Fe, and O elements exist, confirming that the Fe element is present in the doped $SrNiO_3$ perovskite. The C element and other impurity elements are not also found through the EDX analysis, suggesting that the citric acid is obviously decomposed during the heating and calcination process for fabricating the $SrFe_{0.3}Ni_{0.7}O_{2.85}$ perovskite. Moreover, the relative content of elements in $SrFe_{0.3}Ni_{0.7}O_{2.85}$ perovskite can be obtained in Table 4 and the molar ratio of Sr, Ni, Fe, and O elements in the tested material is about 1.00: 0.73: 0.34: 2.58, which is close to the theoretical molar ratio of $SrFe_{0.3}Ni_{0.7}O_{2.85}$ perovskite.

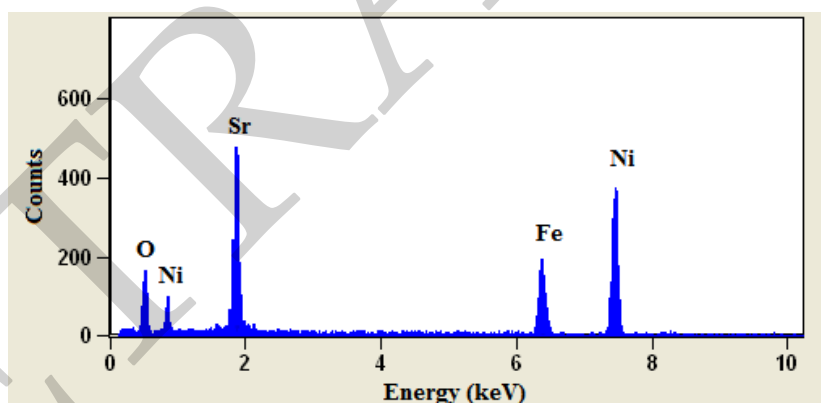**Figure 13.** EDX spectrum of $SrFe_{0.3}Ni_{0.7}O_{2.85}$ perovskite.

Table 4. The relative content of elements in $SrFe_{0.3}Ni_{0.7}O_{2.85}$ perovskite.

Elements	Weight Percent (%)	Atom Percent (%)
Sr	46.02	21.53
Ni	22.44	15.67
Fe	9.85	7.23
O	21.69	55.57
Total	100.00	100.00

3.3.5. Electrochemical Impedance Spectroscopy (EIS) and Tafel Curves Analysis of $SrFe_xNi_{1-x}O_{3-\delta}$

The electrochemical results (EIS and Tafel curves) of $SrFe_xNi_{1-x}O_{3-\delta}$ perovskites present in Figure 14 and their electrochemical parameters (R_{ct} and i_0) are obtained in Table 5. As can be seen

in Figure 14a, the high frequency-region of EIS presents apparent semicircle arcs, and the charge transfer resistance (R_{ct}) of $SrFe_xNi_{1-x}O_{3-\delta}$ (x = 0, 0.1, 0.2, 0.3, 0.4 and 0.5) can be derived from the diameter of the semicircle. The Z'-axis intercepts reflect the solution resistance (R_s) basically fixed at 0.51 Ω cm^2 and the oblique straight lines in low-frequency region represent the Warburg resistance (Z_w) controlled by the electrode diffusion process. The Tafel curves of $SrFe_xNi_{1-x}O_{3-\delta}$ perovskites are shown in Figure 14b, and the asymmetric curves reflect the irreversible redox reaction on the $SrFe_xNi_{1-x}O_{3-\delta}$ perovskites. The i_0 values of Tafel curves can be deduced from the intercepts when the overpotential (η) tends to zero, which relates to the electrocatalytic activity of $SrFe_xNi_{1-x}O_{3-\delta}$ perovskites. In Table 5, the $SrFe_{0.3}Ni_{0.7}O_{2.85}$ perovskite performs the attractive electrocatalytic activity ($i_0 = 891.3 \times 10^{-5}$ mA cm^{-2}) and conductivity (lower R_{ct} value of 7.58 Ω cm^2) among the $SrFe_xNi_{1-x}O_{3-\delta}$ perovskites, which agrees with the electrocatalytic properties (TN removal ratio and conductivity of ECR) in cleaning the nitrogenous wastewater.
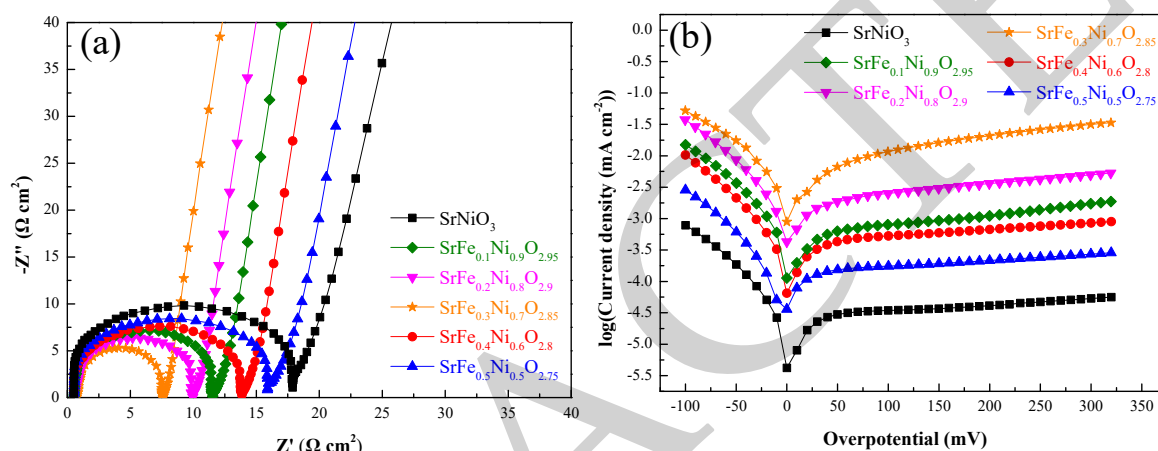

Figure 14. Electrochemical Impedance Spectroscopy (EIS) (**a**) and Tafel curves (**b**) of $SrFe_xNi_{1-x}O_{3-\delta}$.

Table 5. Parameters of $SrFe_xNi_{1-x}O_{3-\delta}$ perovskites.

$SrFe_xNi_{1-x}O_{3-\delta}$ Perovskites	R_{ct} (Ω cm^2)	i_0 (mA cm^{-2})
$SrNiO_3$	17.88	2.570×10^{-5}
$SrFe_{0.1}Ni_{0.9}O_{2.95}$	11.54	54.95×10^{-5}
$SrFe_{0.2}Ni_{0.8}O_{2.9}$	9.97	158.5×10^{-5}
$SrFe_{0.3}Ni_{0.7}O_{2.85}$	7.58	891.3×10^{-5}
$SrFe_{0.4}Ni_{0.6}O_{2.8}$	13.85	37.15×10^{-5}
$SrFe_{0.5}Ni_{0.5}O_{2.75}$	15.88	12.02×10^{-5}

4. Conclusions

In this work, low-cost $SrFe_xNi_{1-x}O_{3-\delta}$ (x = 0, 0.1, 0.2, 0.3, 0.4 and 0.5) perovskites were fabricated using the citrate sol-gel method through doping Fe into the $SrNiO_3$ matrix to improve the conductivity and electrocatalytic activity. In addition, the optimum conditions for fabricating $SrFe_xNi_{1-x}O_{3-\delta}$ perovskites (reaction time of 120 min for citrate sol-gel, a calcination temperature of 700 °C and Fe doping content of x = 0.3) were successively obtained. Then $SrFe_xNi_{1-x}O_{3-\delta}$ perovskites were coated on the Ti plate to prepare the $SrFe_xNi_{1-x}O_{3-\delta}$/Ti electrode. The ECR was built with one $SrFe_xNi_{1-x}O_{3-\delta}$/Ti anode and two stainless steel cathodes to clean nitrogenous wastewater. Furthermore, the characterization results strongly testify to the perovskite-type structure of $SrFe_xNi_{1-x}O_{3-\delta}$. Finally, ECR with the $SrFe_{0.3}Ni_{0.7}O_{2.85}$/Ti anode achieved the attractive TN removal ratio of 91.33% and conductivity of 3.62 mS cm^{-1} in the electrocatalytic process (electrocatalytic time of 150 min). In the optimum conditions, TN concentration in nitrogenous wastewater could be reduced below 15 mg L^{-1} and satisfied the discharge standard of pollutants for municipal wastewater treatment

plants in China (GB 18918-2002, Class I-A Standard, TN $\leq$ 15 mg L^{-1}). Therefore, the SrFe$_x$Ni$_{1-x}$O$_{3-\delta}$ perovskites have a significant and fascinating application for cleaning nitrogenous wastewater.

References

1. Camargo, J.A.; Alonso, A. Ecological and toxicological effects of inorganic nitrogen pollution in aquatic ecosystems: A global assessment. *Environ. Int.* **2006**, *32*, 831. [CrossRef] [PubMed]

2. Bae, B.U.; Jung, Y.H.; Han, W.W.; Shin, H.S. Improved brine recycling during nitrate removal using ion exchange. *Water Res.* **2002**, *36*, 3330–3340. [CrossRef]

3. Xia, G.; Xu, W.; Fang, Q.; Mou, Z.; Pan, Z. Graphene-modulated removal performance of nitrogen and phosphorus pollutants in a sequencing batch chlorella reactor. *Materials* **2018**, *11*, 2181. [CrossRef] [PubMed]

4. Pressley, A.; Bishop, D.F.; Roan, S.G. Ammonia-nitrogen removal by breakpoint chlorination. *Environ. Sci. Technol.* **1972**, *6*, 622–628. [CrossRef]

5. Akira, K.; Guanchen, L.; Michael, V.S.; Yoshihiro, K.; Koichi, K. Modeling the non-equilibrium process of the chemical adsorption of ammonia on gan(0001) reconstructed surfaces based on steepest-entropy-ascent quantum thermodynamics. *Materials* **2017**, *10*, 948. [CrossRef]

6. Huo, S.; Chen, J.; Chen, X.; Wang, F.; Xu, L.; Zhu, F.; Guo, D.; Li, Z. Advanced treatment of the low concentration petrochemical wastewater by Tribonema sp microalgae grown in the open photobioreactors coupled with the traditional Anaerobic/Oxic process. *Bioresour. Technol.* **2018**, *270*, 476–481. [CrossRef] [PubMed]

7. Cardoso, J.C.; Bessegato, G.G.; Zanoni, M.V.B. Efficiency comparison of ozonation, photolysis, photocatalysis and photoelectrocatalysis methods in real textile wastewater decolorization. *Water Res.* **2016**, *98*, 39–46. [CrossRef]

8. Özcan, L.; Mutlu, T.; Yurdakal, S. Photoelectrocatalytic degradation of paraquat by Pt loaded TiO2 nanotubes on Ti anodes. *Materials* **2018**, *11*, 1715. [CrossRef]

9. Okanishi, T.; Katayama, Y.; Muroyama, H.; Matsui, T.; Eguchi, K. SnO$_2$-modified Pt electrocatalysts for ammonia-fueled anion exchange membrane fuel cells. *Electrochim. Acta* **2015**, *173*, 364–369. [CrossRef]

10. Reyter, D.; Bélanger, D.; Roué, L. Nitrate removal by a paired electrolysis on copper and Ti/IrO2 coupled electrodes—influence of the anode/cathode surface area ratio. *Water Res.* **2010**, *44*, 1918–1926. [CrossRef]

11. Pinhedo, L.; Pelegrini, R.; Bertazzoli, R.; Motheo, A.J. Photoelectrochemical degradation of humic acid on a (TiO$_2$)$_{0.7}$(RuO$_2$)$_{0.3}$ dimensionally stable anode. *Appl. Catal. B* **2005**, *57*, 75–81. [CrossRef]

12. Wang, Y.; Cui, X.; Li, Y.; Chen, L.; Shu, Z.; Chen, H.; Shi, J. High surface area mesoporous LaFe$_x$Co$_{1-x}$O$_3$ oxides: Synthesis and electrocatalytic property for oxygen reduction. *Dalton Trans.* **2013**, *42*, 9448–9452. [CrossRef]

13. Shawahni, A.M.; Abu-Jafar, M.S.; Jaradat, R.T.; Ouahrani, T.; Khenata, R.; Mousa, A.A.; Ilaiwi, K.F. Structural, elastic, electronic and optical properties of SrTMO$_3$ (TM = Rh, Zr) compounds: Insights from FP-LAPW study. *Materials* **2018**, *11*, 2057. [CrossRef]

14. Grabowska, E. Selected perovskite oxides: Characterization, preparation and photocatalytic properties—A review. *Appl. Catal. B* **2016**, *186*, 97–126. [CrossRef]

15. Hwang, J.; Rao, R.R.; Giordano, L.; Katayama, Y.; Yu, Y.; Shao-Horn, Y. Perovskites in catalysis and electrocatalysis. *Science* **2017**, *358*, 751–756. [CrossRef]

16. Shi, Z.; Guo, J.; Chen, Y.; Li, Q.; Pan, Y.; Zhang, H.; Xia, Y.; Huang, W. Lead-free organic-inorganic hybrid perovskites for photovoltaic applications: recent advances and perspectives. *Adv. Mater.* **2017**, *29*, 1–28. [CrossRef] [PubMed]

17. Santos-García, A.J.D.; Solana-Madruga, E.; Ritter, C.; Ávila-Brande, D.; Fabeloc, O.; Sáez-Pucheb, R. Synthesis, structures and magnetic properties of the dimorphic Mn_2CrSbO_6 oxide. *Dalton Trans.* **2015**, *44*, 10665–10672. [CrossRef] [PubMed]

18. Mori, D.; Oka, H.; Suzuki, Y.; Sonoyama, N.; Yamada, A.; Kanno, R.; Sumiya, Y.; Imanishi, N.; Takeda, Y. Synthesis, structure, and electrochemical properties of epitaxial perovskite $La_{0.8}Sr_{0.2}CoO_3$ film on YSZ substrate. *Solid State Ionics* **2006**, *177*, 535–540. [CrossRef]

19. Shannon, R.D. Revised effective ionic radii and systematic studies of interatomie distances in halides and chaleogenides. *Acta Cryst.* **2015**, *32*, 751–767. [CrossRef]

20. Ascienzo, D.; Kurt, O.; Greenbaum, S.; Bayer, T.J.M.; Maier, R.A.; Randall, C.A.; Ren, Y. Formation of structural defects and strain in electrodegraded Fe-doped $SrTiO_3$ crystals due to oxygen vacancy migration. *J. Am. Ceram. Soc.* **2018**, *101*, 2545–2561. [CrossRef]

21. Yao, J.; Zhou, M.; Wen, D.; Xue, Q.; Wang, J. Electrochemical conversion of ammonia to nitrogen in non-chlorinated aqueous solution by controlling pH value. *J. Electroanal. Chem.* **2016**, *776*, 53–58. [CrossRef]

22. Zhou, Y.; Zhao, K.; Hu, C.; Liu, H.; Wang, Y.; Qu, J. Electrochemical oxidation of ammonia accompanied with electricity generation based on reverse electrodialysis. *Electrochim. Acta* **2018**, *269*, 128–135. [CrossRef]

23. Vlyssides, A.G.; Karlis, P.K.; Rori, N.; Zorpas, A.A. Electrochemical treatment in relation to pH of domestic wastewater using Ti/Pt electrodes. *J. Hazard. Mater.* **2002**, *B95*, 215–226. [CrossRef]

24. Oskoui, S.A.; Niaei, A.; Tseng, H.H.; Salari, D.; Izadkhah, B.; Hosseini, S.A. Modeling preparation condition and composition-activity relationship of perovskite-type $La_xSr_{1-x}Fe_yCo_{1-y}O_3$ nano catalyst. *ACS Comb. Sci.* **2013**, *15*, 609–621. [CrossRef] [PubMed]

25. Zhang, C.; Guo, Y.; Guo, Y.; Lu, G.; Boreave, A.; Retailleau, L.; Baylet, A.; Giroir-Fendler, A. $LaMnO_3$ perovskite oxides prepared by different methods for catalytic oxidation of toluene. *Appl. Catal. B* **2014**, *148–149*, 490–498. [CrossRef]

26. Xu, L.; Xin, Y.; Wang, J. A comparative study on IrO_2-Ta_2O_5 coated titanium electrodes prepared with different methods. *Electrochim. Acta* **2009**, *54*, 1820–1825. [CrossRef]

27. Wang, G.; Gao, J.; Fu, L.; Zhao, N.; Wu, Y.; Takamura, T. Preparation and characteristic of carbon-coated Li4Ti5O12 anode material. *J. Power Sources* **2007**, *174*, 1109–1112. [CrossRef]

28. Vidal-Iglesias, F.J.; Garcia-Araez, N.; Montiel, V.; Feliu, J.M.; Aldaz, A. Selective electrocatalysis of ammonia oxidation on Pt (100) sites in alkaline medium. *Electrochem. Commun.* **2003**, *5*, 22–26. [CrossRef]

29. China Standards Publication. *Discharge Standard of Pollutants for Municipal Wastewater Treatment Plant in China*; GB 18918-2002; China Standards Press: Beijing, China, 2002.

30. China Standards Publication. *Alkaline Potassium Persulphate Digestion UV Spectrophotometric Method*; HJ 636-2012; China Standards Press: Beijing, China, 2012.

31. Li, B.; Tang, C.; Wang, H.; Zhu, X.; Zhang, Q. An aqueous preoxidation method for monolithic perovskite electrocatalysts with enhanced water oxidation performance. *Sci. Adv.* **2016**, *2*, e1600495. [CrossRef]

32. Hancock, C.A.; Slater, P.R. Synthesis of silicon doped SrMO3 (M = Mn, Co): stabilization of the cubic perovskite and enhancement in conductivity. *Dalton Trans.* **2011**, *40*, 5599–5603. [CrossRef]

33. Tsuruta, A.; Nomura, K.; Mikami, M.; Kinemuchi, Y.; Terasaki, I.; Murayama, N.; Shin, W. Unusually small thermal expansion of ordered perovskite oxide $CaCu_3Ru_4O_{12}$ with high conductivity. *Materials* **2018**, *11*, 1650. [CrossRef] [PubMed]

34. Weng, S. *Fourier Transform Infrared Spectroscopy*; Chemical Industry Press: Beijing, China, 2010; pp. 377–389.

35. Wu, T.; Xu, Z.; Zhang, Y.; Wang, H.; Cui, C.; Chang, B.; Feng, X.; Liu, W. A pH-responsive biodegradable high-strength hydrogel as potential gastric resident filler. *Macromol. Mater. Eng.* **2018**, *303*, 1800290. [CrossRef]

36. Kim, Y.Y.; Dong, H.L.; Kwon, T.Y.; Park, S.H. Infrared spectra and seebeck coefficient of $LnCoO_3$ with the perovskite structure. *J. Solid State Chem.* **1994**, *112*, 376–380. [CrossRef]

37.	Zhu, J.; Xiao, D.; Li, J.; Yang, X.; Wu, Y. Effect of Ce on NO direct decomposition in the absence/presence of O2 over $La_{1-x}Ce_xSrNiO_4$ ($0 \leq x \leq 0.3$). *J. Mol. Catal. A* **2005**, *234*, 99–105. [CrossRef]

38.	Wang, H.; Li, G.; Li, L. Molten-salt-mediated synthesis and low-temperature electrical conduction of $LnCoO_3$ (Ln = Pr, Nd, Sm, and Gd). *J. Alloys Compd.* **2014**, *612*, 227–232. [CrossRef]

39.	Ratheesh, R.; Sreemoolanadhan, H.; Sebastian, M.T. Vibrational analysis of $Ba_{5-x}Sr_xNb_4O_{15}$ microwave dielectric ceramics resonators. *J. Solid State Chem.* **1997**, *131*, 2–8. [CrossRef]

40.	Ye, S.; Wang, C.; Jing, X. Photoluminescence and Raman spectra of double-perovskite $Sr_2Ca(Mo/W)O_6$ with A-and B-site substitutions of Eu^{3+}. *J. Electrochem. Soc.* **2008**, *155*, J148–J151. [CrossRef]

41.	Fu, M.; Liu, X.; Chen, X. Raman spectra analysis for $Ca(B'_{1/3}B''_{2/3})O_3$-based complex perovskite ceramics. *J. Appl. Phys.* **2008**, *104*, 1182. [CrossRef]

42.	Caracas, R.; Cohen, R.E. Theoretical determination of the Raman spectra of $MgSiO_3$ perovskite and post-perovskite at high pressure. *Geophys. Res. Lett.* **2006**, *33*, 229–237. [CrossRef]

43.	Ksepko, E. Perovskite-type $Sr(Mn_{1-x}Ni_x)O_3$ materials and their chemical-looping oxygen transfer properties. *Int. J. Hydrogen Energy* **2014**, *39*, 8126–8137. [CrossRef]

44.	Zinkevich, M. Constitution of the Sr-Ni-O system. *J. Solid State Chem.* **2005**, *178*, 2818–2824. [CrossRef]

45.	Sun, Z.; Yuan, H.; Liu, Z.; Han, B.; Zhang, X. A highly efficient chemical sensor material for H_2S: α-Fe_2O_3 nanotubes fabricated using carbon nanotube templates. *Adv. Mater.* **2005**, *17*, 2993–2997. [CrossRef]